

Characterization of a new variable magnetic field linear plasma device

Cite as: Phys. Plasmas **28**, 123514 (2021); <https://doi.org/10.1063/5.0070924>

Submitted: 10 September 2021 • Accepted: 16 November 2021 • Published Online: 09 December 2021

 F. Filleul,  A. Caldarelli,  C. Charles, et al.



View Online



Export Citation



CrossMark

Physics of Plasmas

Papers from 62nd Annual Meeting of the
APS Division of Plasma Physics

Read now!

AIP
Publishing

Characterization of a new variable magnetic field linear plasma device

Cite as: Phys. Plasmas **28**, 123514 (2021); doi: [10.1063/5.0070924](https://doi.org/10.1063/5.0070924)
Submitted: 10 September 2021 · Accepted: 16 November 2021 ·
Published Online: 9 December 2021



View Online



Export Citation



CrossMark

F. Filleul,^{1,a)}  A. Caldarelli,²  C. Charles,³  R. W. Boswell,³  N. Rattenbury,¹  and J. Cater² 

AFFILIATIONS

¹Te Pūnaha Ātea-Auckland Space Institute, Department of Physics, The University of Auckland, Auckland 1010, New Zealand

²Te Pūnaha Ātea-Auckland Space Institute, Department of Engineering Science, The University of Auckland, Auckland 1010, New Zealand

³Space Plasma, Power and Propulsion Laboratory, Research School of Physics, The Australian National University, Canberra ACT 2601, Australia

^{a)}Author to whom correspondence should be addressed: felicien.filleul@auckland.ac.nz

ABSTRACT

A radio frequency plasma device is presented in which the regions of plasma creation and maximum plasma magnetization can be separated along a 1.5-m tube. Measurements of the plasma density, plasma potential, and electron temperature in the device successfully reproduce previously reported plasma features. These validate the ability of the experiment to continue the investigation of a regime of operation in which the axial plasma density follows the profile of the applied magnetic field, as long as the ions are magnetized under the antenna. The density is shown to increase on axis owing to the decreasing cross section of the converging magnetic funnel connecting the antenna region to the solenoids. When the funnel pinching is increased, stronger magnetic fields are required to inhibit cross-field diffusion and to bring the density on axis in the expected 10^{12} cm^{-3} range. Collisionless transport of hot electron populations is observed along the field lines which intersect the area under the antenna and coincides with the presence of high-density conics more than 0.5 m away from the antenna for magnetic fields $\geq 600 \text{ G}$.

Published under an exclusive license by AIP Publishing. <https://doi.org/10.1063/5.0070924>

I. INTRODUCTION

Linear magnetized plasma devices have played an important role in the understanding of many plasma phenomena and the development of technologies, ranging from wave-heated plasmas,^{1,2} to open ended early fusion experiments,³ neutral-beam injection heating for Tokamaks,⁴ to astrophysical plasmas,^{5,6} and more recently to electric spacecraft propulsion.⁷ Of particular interest are electric propulsion concepts that rely on electrodeless radio frequency (rf) sources for plasma creation and a converging-diverging magnetic field geometry, also called a magnetic nozzle (MN), for plasma acceleration. Examples of such concepts are the helicon double-layer thruster and the magnetic nozzle rf thruster, whose development have progressed in the last twenty years.^{8,9} Because a magnetic nozzle provides a significant portion of the total thrust and contributes to increase the thruster efficiency, a better understanding of particle transport and thermodynamics along the magnetic field lines is key to improving the performances of these thrusters.^{10,11} For example, the creation of supersonic ion beams has been associated with the existence of high plasma density conical structures downstream of the magnetic nozzle throat.^{12–16}

These conics are themselves due to the transport of high energy electrons along magnetic field lines exiting the thruster.

Most of the experimental devices used for studying such phenomena have fixed plasma source and magnetic nozzle locations, making the study of the effects of the magnetic field topology difficult.^{8,17,18} To address this, a set of two linear plasma devices have been created in which the region of plasma creation and maximum magnetic field can be separated. The first results on a device located in Australia have exhibited two modes of operation depending on the distance between these two regions.¹⁹ In the first mode, the axial plasma density is maximum at the throat of the magnetic nozzle (MN) and follows it as it is moved away from the antenna. In the second mode, the axial density peaks both under the antenna and under the MN when separated beyond a critical distance. These modes have been related to the level of ion magnetization along the plasma column and to the transport of hot electrons. To pursue and expand the investigation started in Australia, a second linear plasma device has been manufactured in Aotearoa New Zealand. This device closely reproduces the first, except for the operating radio frequency range and the

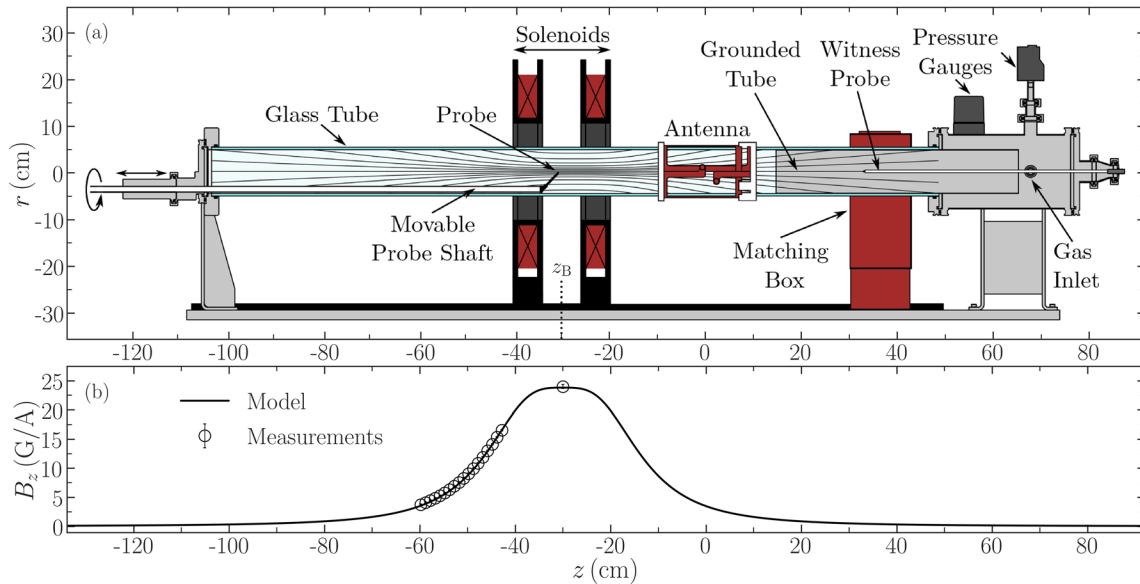


FIG. 1. (a) Schematic of the *Huia* device with main components labeled. The double-saddle (DS) antenna is centered at $z = 0$ cm and the movable solenoid pair is centered at $z = z_B = -30$ cm in the present case. The movable probes are inserted through a linear/rotary vacuum feedthrough at $z = -110$ cm. (b) Calculated axial magnetic field strength B_z for a solenoid current of 1 A (solid line) and comparison with Hall effect probe measurements (circle markers).

use of different antenna geometries. This study presents the design, characterization, and first results obtained with this new experiment. The results independently confirm the findings of Bennet *et al.*¹⁹ and bring new insights into the magnetized energized electron transport.

II. THE HUIA LINEAR PLASMA DEVICE

The new device was named *Huia* after an extinct New Zealand native bird. It has been designed as a complementary setup to the *Echidna* plasma experiment located at the Australian National University.¹⁹ *Huia*'s main features are represented in Fig. 1(a) and compared to *Echidna*'s in Table I. The two experiments are identical in size and electrical material properties, with the active region being a 150-cm-long, 9-cm-inner diameter borosilicate glass tube extending from a 27-cm-long, 15-cm inner diameter stainless steel vacuum chamber. A 250 l/s turbo pump is backed by a 24 m³/h primary pump to achieve a base pressure of a few 10^{-7} Torr, as monitored by a full-range cold cathode/Pirani gauge. The working pressure using argon is between 10^{-4} and 10^{-2} Torr, as measured by a capacitance diaphragm gauge. Argon is injected at $z = 68$ cm and regulated by a 0.1–100 sccm mass-flow controller. Pressure measurements upstream and downstream of the glass tube using the capacitance diaphragm gauge have shown the absence of a pressure gradient along the tube over the entire range of mass-flow rate. The results presented were all obtained at

TABLE I. *Huia* and *Echidna*¹⁹ comparison.

| Device | Length and \varnothing (cm) | Freq. (MHz) | Antenna |
|----------------|-------------------------------|-------------|--------------------|
| <i>Huia</i> | 150 and 9 | 27.12 | Double-saddle/loop |
| <i>Echidna</i> | 150 and 9 | 13.56 | Double-saddle |

10 sccm of argon, which corresponds to a working pressure of 1 mTorr.

The rf power from a 1 kW, 25–42 MHz rf generator is either fed to a 19 cm long double-saddle (DS) antenna,¹ identical to the one used on *Echidna*, or a 1–1/3 turns tightly wound loop antenna. The center of the double-saddle antenna is the origin of the (r, z) reference frame, which also corresponds to the position of the loop antenna when in use. The impedance of the ensemble (transmission line + antenna + plasma) is matched to the rf generator 50 Ω output using an L-type matching network. This study was conducted at 27.12 MHz instead of the 13.56 MHz used on *Echidna*. A grounded 89-mm outer diameter thin aluminum tube is inserted inside the glass tube up to $z = 15$ cm to serve as a ground reference for the plasma close to the antenna to avoid instabilities.¹⁹

A pair of solenoids was designed with the same dimensions as the pair used on *Echidna*, i.e., an inner coil radius of 11 cm and a coil thickness of 4 cm. Each coil winding consists of 352 turns of a 3 mm enameled copper wire. The pair produces a maximum magnetic field strength of 23.82 G/A on axis when set 14 cm apart center to center. The position of the solenoids is controlled by a stepper motor and can range from $z = 10$ to $z = -80$ cm allowing a wide range of magnetic field configurations. The axial coordinate of the center of the solenoids is denoted as z_B , which also corresponds to the location of maximum axial magnetic field strength B_{z_B} . The two-dimensional magnetic field is calculated using an analytical solution of the spatial field created by single loops of current.²⁰ The calculated axial magnetic field strength B_z is compared with measurements acquired with a single axis Hall effect probe in Fig. 1(b) and shows good agreement.

III. DIAGNOSTICS

The development of *Huia* was simultaneous with the design, manufacturing, and testing of dedicated *in situ* electrostatic diagnostics

and controlling electronics. The results presented in this study were obtained with three Langmuir probes (LP) and one emissive probe (EP), reproducing as closely as possible the apparatus and methodology used by Bennet *et al.* on *Echidna*.¹⁹ As illustrated in Fig. 1(a), the probe assemblies are mounted at the extremity of an off-center 1.5 m long probe shaft inserted at the downstream end of *Huia* ($z = -120$ cm). The probe assemblies are made with a thin ceramic tube doglegged at 15° with respect to the axis of the movable probe shaft. The sensing head of the probe is placed at the extremity of the ceramic tube and its position is labeled (r_p, z_p) . The axial and azimuthal motions of the movable probe shaft are controlled by two stepper motors, giving access to the properties of the entire axisymmetric plasma column. Rotating this shaft by $\pm 75^\circ$ moves the probe head from its axial position ($r_p = 0$ cm) to the edges of the glass tube ($r_p = 4.3$ cm). The electrical properties and dimensions of the movable probe shaft have been subject to an iterative design process aimed at minimizing the disturbance to the plasma column.

Two LPs are used for spatial ion density, floating potential, and electron temperature measurements. A single-sided 2-mm-diameter nickel disk mounted at the end of a 2-mm-diameter ceramic tube is used to measure the ion saturation current by biasing it at -100 V with respect to ground in order to ensure electron rejection. The probe radius was chosen to be smaller than the ion Larmor radius everywhere in the plasma to neglect magnetic effects of the ion orbital motion to the probe. The same probe can remain floating to record the plasma floating potential. A cylindrical Langmuir probe made of a 0.25-mm-diameter, 5-mm-long tungsten wire and kept perpendicular to the applied axial magnetic field is used to measure the electron temperature T_e . The radius of the probe was also selected to avoid magnetized electron orbital motion effects on the collected current. The probe voltage bias is swept to acquire a current-voltage trace, and T_e is obtained by finding the slope of electron current between the floating and plasma potentials on a semi-log scale.²¹ The sweeping bias is produced by amplifying 10 periods of a 10 Hz triangle wave from the analog output of a Data Acquisition (DAQ) unit with a custom-made bipolar power amplifier which can output up to ± 140 V. The use of a triangle wave bias allows a systematic check for hysteresis in the probe trace, which could be a sign of probe contamination or a change in work function.²² The current collected by the probe is obtained by measuring the voltage drop across a variable measurement resistor R_m with a custom-made low-noise isolation amplifier circuit and recorded by the DAQ. The 20 current-voltage traces are then averaged before extracting T_e . Knowing the electron temperature, one can then obtain the ion density n_i from the ion saturation current I_{sat} measured with the planar probe using

$$I_{\text{sat}} = 0.61eA_p u_B n_i, \quad (1)$$

where e is the elementary charge magnitude, A_p the probe surface area, and $u_B = \sqrt{kT_e/m_i}$ the Bohm speed, respectively, with k the Boltzmann constant and m_i the ion mass.^{21,23,24} In discharges with a notable capacitive coupling, such as those studied here, the lack of rf compensation is known to result in an overestimation of the electron temperature.²⁵ Overestimating the electron temperature has a limited effect in the density calculation, because the plasma density is proportional to the square root of T_e . Therefore, possible errors caused by the lack of rf compensation were judged not to be detrimental to this study, since the principal focus concerns a relative comparison of

plasma densities. Additionally, the present method of plasma density determination does not take into account the effect of the probe sheath expansion, and can result in the overestimation of the absolute density.²⁶ The results reported on *Echidna* used the same method with a probe of similar dimensions; thus, the overestimations should be comparable.¹⁹ A third stationary 3-mm-diameter disk Langmuir probe kept at $z = 28$ cm is used as a witness probe, measuring the plasma floating potential to check for plasma disturbance while inserting and removing the movable probe shaft, see Fig. 1.

The emissive probe consists of a 0.127-mm-diameter U-shaped tungsten wire inserted into a ceramic tube with two bore holes mounted on the movable probe shaft. The wire is heated to electron emission by a direct current from a power supply isolated from ground by an isolation transformer. The local plasma potential is measured using the floating potential method; by recording the probe floating potential as a function of the heating current with the DAQ, the knee of the potential-current trace is observed near the plasma potential.²⁷ Typical measurement errors inherent to the floating potential method are due to the voltage drop across the full length of the tungsten wire, here ~ 3.5 V, combined with a knee location uncertainty of ± 1 V, for a total error of ± 2.75 V. Plasma potentials acquired with the EP have been compared with measurements recorded with a retarding field energy analyzer under multiple plasma conditions and have shown good agreement.²⁸

IV. RESULTS

All of the reported data were obtained at 1 mTorr of argon and, unless otherwise specified, at $P_{\text{rf}} = 200$ W with the reflected power kept below 1% and with a solenoid current of 12.6 A, producing a maximum magnetic field strength on axis of 300 G. The relatively low rf power was chosen to protect the probes from overheating damage, to reduce the sputtering of surfaces in contact with the plasma, and to conduct measurements under similar conditions to the results previously published in Ref. 19. Furthermore, these results reported that the plasma dynamics of interest were not correlated with the rf power in the range 200–1000 W.

A. Discharge characterization and probe disturbance mitigation

One of the surprising results observed on *Echidna* was the absence of measured helicon waves despite observing a blue core and plasma densities in excess of 10^{12} cm⁻³, which are typically associated with the helicon regime.^{1,19} As a B-dot probe was not available at the time of this study to test the presence of helicon waves in *Huia*, an alternative was to use the planar Langmuir probe to monitor the change in ion saturation current with the applied rf power to look for mode transitions. This was performed by placing the probe on axis under the double-saddle antenna, with the solenoids placed on top of the antenna, such that $z_p = z_B = 0$ cm. Figure 2 shows the normalized ion saturation currents obtained for rf powers over the entire available range in steps of 50 W. The curve shows a square-root dependency for rf powers below 300 W, which is commonly attributed to a capacitive coupling of the antenna with the plasma (E-mode),^{29,30} Above 300 W, I_{sat} increases linearly with rf power, matching the expected trend of the inductive mode (H-mode).³¹ Wave heating mode onset often manifests itself by a step increase in I_{sat} with rf power.^{24,32} Figure 2 shows no such step increase, nor was it observed over the

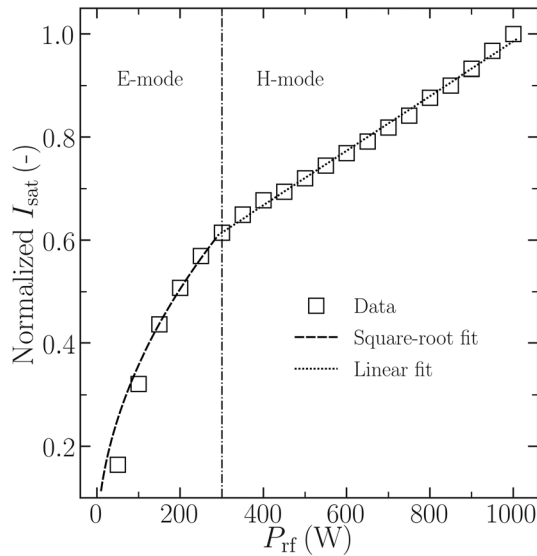


FIG. 2. Normalized I_{sat} as a function of the rf power applied to the double-saddle antenna showing mode transition at $P_{\text{rf}} \approx 300$ W. I_{sat} was measured with the planar LP under the antenna at $(r, z) = (0, 0)$ cm with $z_{\text{B}} = 0$ cm and 300 G.

entire range of experimental conditions, giving evidence that wave heating modes are not predominant in *Huia*. Nevertheless, similar to what has been observed on *Echidna*, blue cores were observed at either higher rf power, magnetic field strengths, and increasing distance between the antenna and the solenoids, or a combination of these factors.

A focus of the characterization campaign conducted in *Huia* was the mitigation of the discharge disturbance induced by the insertion of the movable probe shaft into the plasma column. The first design of this shaft was an electrically grounded 12-mm-diameter stainless steel tube which came supplied with the commercial vacuum linear/rotation motions feedthrough. It was observed that the insertion of this shaft changed the argon emission color from a blue-purple to pink when the solenoids were at $z_{\text{B}} = -30$ cm and with $P_{\text{rf}} \geq 200$ W and magnetic fields ≥ 300 G. The matching was also affected as the shaft was brought closer to the antenna. The disturbance was further quantified by measuring the plasma floating potential variation at the fixed location $z = 28$ cm with the witness probe during the movable probe insertion. This is shown in Fig. 3, where the witness probe floating potential V_f progressively decreases before abruptly increasing when the movable probe reaches the antenna region, in accordance with the observed change in matching conditions.

The vacuum feedthrough was subsequently modified to accommodate a 6.35-mm-diameter steel shaft, and the measurements were repeated. Figure 3 shows that this design did not reduce the disturbance. The third design iteration used a 10-mm borosilicate tube as a sheath surrounding the 6.35-mm steel shaft. This glass tube was sealed to the shaft at its atmosphere exposed end using vacuum compatible epoxy. The mounting mechanism of the probes at the other end of the shaft was modified to ensure that no grounded metallic surfaces came in contact with the plasma. In Fig. 3, it can be seen that the floating potential still drops by ~ 4 V over the first 10 cm of inserting the probe but stays approximately constant (± 0.5 V) over the remainder of the column, even in the antenna region. Simultaneously,

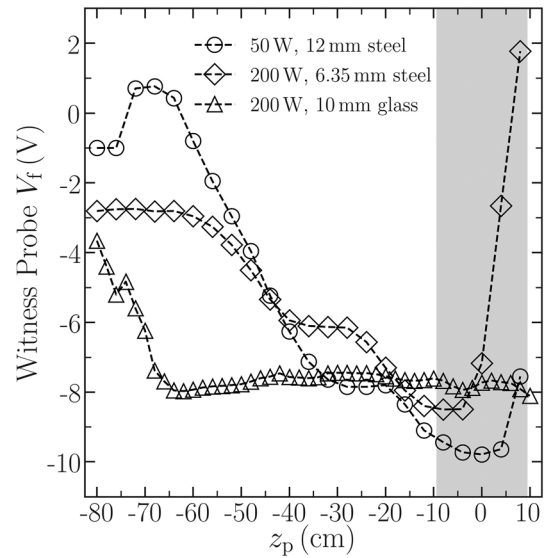


FIG. 3. Plasma floating potential measured by the witness probe at the fixed location $(r, z) = (0, 28)$ cm as a function of the movable probe position z_p , for three different movable probe shafts, obtained for $z_{\text{B}} = -30$ cm, 300 G with the double-saddle antenna. The shaded area marks the extent of the DS antenna.

the argon emission color was not affected by the presence of the glass-covered shaft and the matching remained constant upon shaft insertion. Because only relative spatial potential changes would affect the dynamics of the plasma species, the absolute ~ 4 V offset over the region of interest is expected to have a negligible impact on the plasma characterization. Therefore, this probe shaft design was deemed suited to take reliable measurements.

Bennet *et al.*¹⁹ hypothesized the role of wall charging in the efficient transport of electrons heated up under the antenna region to the solenoids.¹⁹ Therefore, the observed effects of inserting a conductive or dielectric shaft into the plasma could be attributed to modification of the equilibrium of charged species fluxes to the boundaries, resulting in plasma potential variations. The reduction of the plasma disturbance in terms of spatial potential, emission color, and matching stability, by switching from a conductive shaft to a dielectric one, is an argument supporting the role of wall charging in *Huia*/*Echidna*. However, the role of other mechanisms, such as spurious coupling between the shaft and the antenna, or increase in the plasma loss surface area, cannot be ruled out.

B. Double-saddle and loop antennae comparison

The next step focused on confirming that *Huia* could reproduce the behaviors observed in *Echidna*, despite *Huia* working at a different radio frequency (27.12 vs 13.56 MHz). The principal result reported in Ref. 19 was the existence of two modes of operation as the location of plasma heating and the location of the strongest magnetic field were progressively separated: a single-peaked mode where the plasma density is maximum under the solenoids and a double-peaked mode in which the density peaks both under the antenna and under the solenoids.¹⁹ These regimes were tested in *Huia* by using a double-saddle antenna identical to the one employed in *Echidna*.

Figure 4 displays the axial density profiles for z_B decreasing in 10 cm steps from $z_B = 0$ cm to -60 cm. The density is calculated using Eq. (1), where I_{sat} is obtained with the planar Langmuir probe and T_e with the cylindrical Langmuir probe. For the double-saddle antenna (DS), the measurements of electron temperature performed on *Huia* showed axial variations with a standard deviation of 0.5 eV about an axial average of 5.5 eV. However, Bennet *et al.*¹⁹ reported a constant electron temperature on axis. This discrepancy is attributed

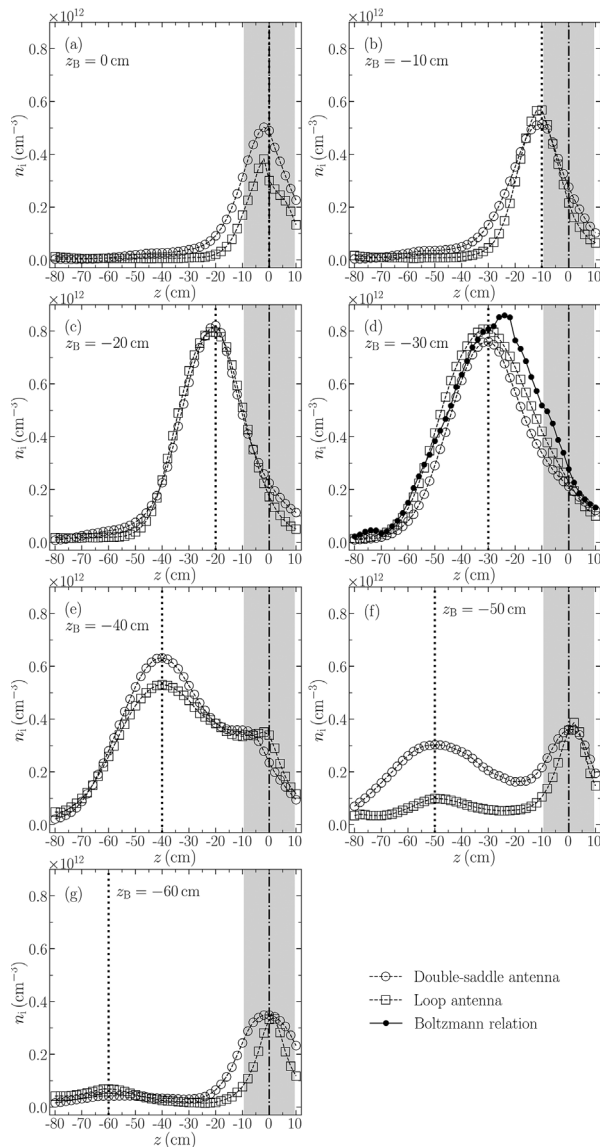


FIG. 4. Axial ion density profiles as the distance between the solenoids and the antennae (z_B , vertical dotted line) is increased in steps of 10 cm, from (a)–(g). Circle markers are for the double-saddle antenna (shaded area) while square markers are for the loop antenna (vertical dash-dotted line). The shaded area marks the extent of the DS antenna, the dash-dotted line the position of the loop antenna. The filled markers in (d) show the Boltzmann relation [Eq. (2)] tested for the loop antenna. The conditions are: $P_{\text{rf}} = 200$ W and 300 G.

to the lack of rf compensation, and the value of $T_e = 5.5$ eV is used for the calculations of n_i . Throughout this study, electron populations with temperatures below and above 5.5 eV are referred to as cold and hot, respectively. Figure 4 shows a regime transition from an ion density profile exhibiting a single peak under the solenoids for $z_B \in [-30; 0]$ cm to double-peaked profiles for $z_B \leq -40$ cm. The plasma potential axial profile for the double-saddle antenna obtained with the emissive probe when $z_B = -30$ cm is also reported in Fig. 6. It shows a single peak at the solenoids location with a monotonic decrease on each sides, matching the ion density trend. This V_p would attract electrons and repel ions from either sides of the peak. Similar behaviors were reported in Ref. 19, indicating that *Huia* is suited to continue and complement the research started on *Echidna*.

Some differences are nevertheless present. In Fig. 4, a global maximum density of $8.17 \times 10^{11} \text{ cm}^{-3}$ is produced for $z_B = -20$ cm that remains nearly stable until $z_B = -30$ cm. In contrast, *Echidna* displayed a density increasing from $\sim 6 \times 10^{11} \text{ cm}^{-3}$ to $\sim 9 \times 10^{11} \text{ cm}^{-3}$ between $z_B = -20$ cm and -30 cm. The axial plasma potential profile reported in Fig. 6 also has a global negative offset of approximately 10 V compared to that measured on *Echidna*. The cause of these differences in absolute densities and plasma potential between *Huia* and *Echidna*, as well as the density peaking when $z_B = -20$ cm instead of $z_B = -30$ cm, are not known. A possible explanation could be the use of a movable probe shaft which presents a floating dielectric boundary to the plasma compared to the earthed steel shaft used in *Echidna*. It is also likely that the measurement uncertainties overlap between the two experiments due to similar measurement method uncertainties, as described in Sec. III.

Bennet *et al.*¹⁹ linked the regime transition occurring between $z_B = -30$ cm and -40 cm to the degree of ion magnetization under the antenna; i.e., when the ion Larmor radius $r_{Li} = \sqrt{m_i v_{\text{ith}} / e B_z}$, where v_{ith} is the ion thermal velocity, becomes larger than the glass tube inner radius of 4.5 cm as the solenoids are moved away from the antenna. Assuming ions at room temperature results in $v_{\text{ith}} = 394$ m/s, so that r_{Li} at $z = 0$ cm increases from ~ 3.7 to ~ 8 cm when the solenoids are moved from $z_B = -30$ to -40 cm and equals 4.5 cm for $z_B \simeq -32.4$ cm. This transition in ion magnetization is depicted in Fig. 5 for ions on axis, for simplicity. As more ions intersect the glass tube during their gyromotions for $z_B < -32.4$ cm, their contribution to the charging of the glass tube under the antenna increases, making the wall more positive and resulting in a potential well trapping the hot electrons created a few rf skin depths under the antenna, as illustrated in Fig. 5(b). These electrons would have otherwise traveled downstream along the field lines to contribute to the local ionization under the solenoids in the single peak regime.¹⁹ One problem with the experimental configuration used so far is the 19-cm axial extent of the double-saddle antenna. Indeed, when the solenoids are at $z_B = -40$ cm, r_{Li} remains smaller than the glass tube radius under the downstream extremity of the antenna at $z = -9.5$ cm, and this results in an indistinct regime transition. The double-saddle antenna was therefore replaced with a loop antenna with an axial extent of ~ 0.5 cm. With the current understanding that wave heated regimes are not noticeably contributing to the plasma production in *Huia/Echidna*, this change of antenna should not affect the dynamics of interest.

Figure 4 shows the axial n_i profiles for the loop antenna. The average T_e on axis was measured to be 5.4 eV, which is close to the

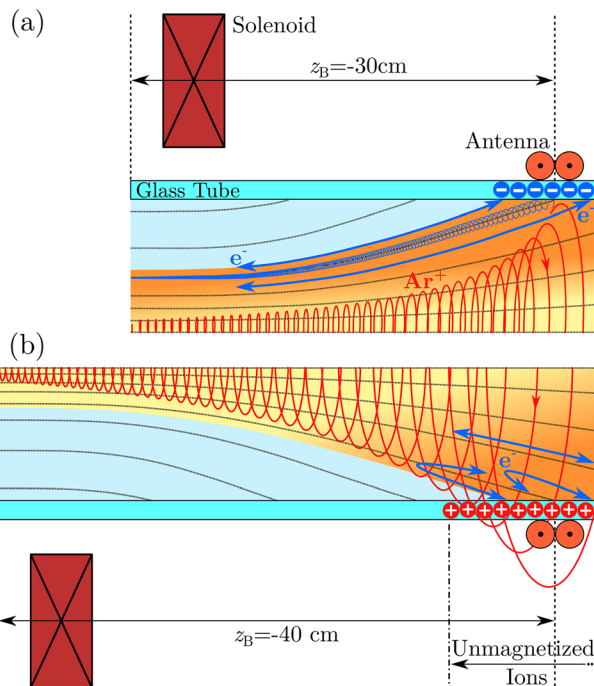


FIG. 5. Illustration showing the effect of the ions' Larmor motion (red helices) on the charging of the glass tube, and the resulting downstream transport and upstream confinement of the electrons (blue arrows and helix), for $z_B = -30$ (a) and $z_B = -40$ cm (b). The light blue shaded regions represent the cold electron population that cannot access the antenna heating region. The yellow to red gradient indicates the warmer electron population. The latter is heated a few skin depths under the antenna and then either transported downstream (a) or confined under the antenna by the positive wall charging (b). The regions of negative and positive charging of the wall are indicated by the blue circles with negative signs (a) and by the red circles with positive signs (b), respectively. The pair of large orange circles represent the loop antenna position. The ion and electron Larmor radii are drawn to scale.

temperature measured for the double-saddle antenna. The density profiles are strikingly similar to those of the DS antenna, peaking exactly at the same locations and with comparable magnitudes for the $z_B = -10$ to -30 cm cases. These matching plasma densities and electron temperatures show that the heating regime in *Huia* was unaffected by the change of antenna. For $z_B = -40$ cm, the peak under the solenoids has a lower magnitude compared to that measured with the DS antenna. For $z_B = -50$ cm, the peak under the solenoids is more than 3 times lower than the DS antenna one, while the profiles match again for $z_B = -60$ cm. These observations are additional evidence that the ion magnetization under the antenna plays an important role in the regime transition. Indeed, for $z_B = -40$ and -50 cm, the extent of the DS antenna makes it more probable for hot electrons to be still channeled down the magnetic field lines despite the local wall charging reducing the amount of electrons with sufficient kinetic energy to overcome the potential well. With the loop antenna, not enough hot electrons are reaching the solenoids to create a significant density peak at $z_B = -50$ cm.

Figure 6 shows V_p for the loop antenna when $z_B = -30$ cm; this profile is similar to the one obtained with the DS antenna with a global

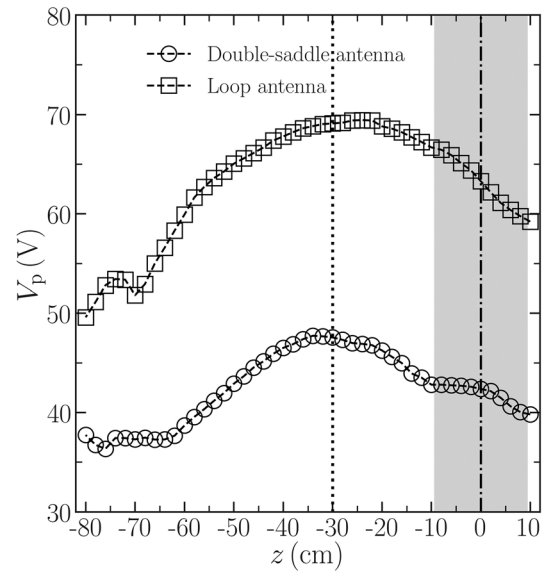


FIG. 6. Axial plasma potential profiles for the double-saddle antenna (circle markers) and the loop antenna (square markers) for $z_B = -30$ cm (dotted vertical line). Both profiles peak around z_B , coinciding with the ion density peak location in Fig. 4(d).

positive offset of ~ 20 V whose cause is unknown. Since the offset does not affect the potential gradients, it has no effect on the forces experienced by the charged plasma species on axis. In particular, the potential increase in 5.8 V between the antenna and the solenoids is close to the 5.2 V observed with the DS antenna. As highlighted in Ref. 19, this gradient creates an axial electrostatic force that negates the adiabatic reflection of electrons by the strong magnetic mirror ratio created in this condition. With the solenoids at $z_B = -30$ cm, the average magnetic mirror force between $z = 0$ cm and z_B is $\sim 2.94 \times 10^{-18}$ N.³³ For the DS and loop antennae, the mean electrostatic forces are $\sim 2.77 \times 10^{-18}$ and $\sim 3.11 \times 10^{-18}$ N, respectively, closely balancing the magnetic mirror force.

Overall, the similarities of the axial density and plasma potential profiles of the DS and loop antennae show that employing a different source of primary ionization maintains the dynamics of interest for this study and will allow a more precise discrimination of the conditions for regime transition.

C. Plasma behavior for $z_B = -30$ cm

Figure 7 shows the radial profiles of the plasma parameters taken under the antenna ($z_p = 0$ cm) and under the solenoids ($z_p = z_B = -30$ cm), for both antennae. The dashed vertical lines mark the radial position of the most outward field lines under the solenoids which still intersect the glass surface under the antenna: $r \simeq 2.6$ and 1.7 cm for the DS and loop antennae, respectively. This reduction in radius is owing to the loop antenna bringing the region of electron heating about 9 cm more upstream than the DS antenna [see field lines in Fig. 1(a)]. The density profiles are similar for the two antennae; both exhibit a factor of ~ 3 axial increase between the antenna and the solenoids and a monotonic decrease from center to edge.

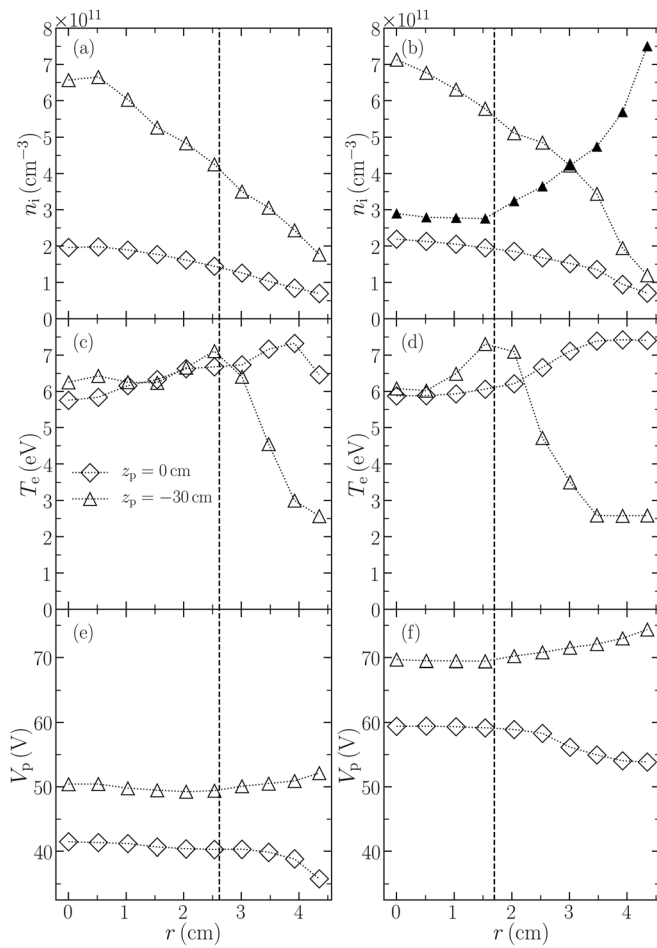


FIG. 7. Radial profiles of the plasma parameters n_i , T_e , and V_p for the double-saddle antenna (a), (c), and (e) and loop antenna (b), (d), and (f), obtained with the solenoids at $z_B = -30$ cm. Diamond markers are for radial profiles under the antenna ($z_p = 0$ cm) while the triangle markers are for profiles under the solenoids ($z_p = z_B = -30$ cm). The filled marker curve shown in (b) is a test of the Boltzmann relation [Eq. (2)] for $z_p = -30$ cm. The dashed vertical lines show the position of the most radial magnetic field line that still intersects the antennae.

The significant density increase on axis compared to the nearly constant values on the edge is a consequence of plasma magnetic confinement, as it will be discussed later.

The V_p profile trends in Figs. 7(e) and 7(f) are also identical for the two antennae besides the ~ 20 V offset already shown in Fig. 6. Under the antenna, V_p decreases from the center to the edge by ~ 5.5 V in both cases. Associating this trend in V_p with the behavior of T_e under the antenna through the equation $V_f \simeq V_p - 5.2T_e$ results in a net decrease in V_f from center to edge by ~ 11 V.²³ Because the electron Larmor radius r_{Le} is on the order of 1 mm under the antenna, electrons are trapped along the field lines that intersect the glass tube under the antenna. This causes the wall at this location to charge negatively compared to the bulk plasma as electrons orbiting these field lines are lost to the wall during the initial plasma breakdown phase. This is illustrated in Fig. 5(a) with the small electron

gyromotion around a field line intersecting the wall under the antenna. The radial plasma potential profile then adjusts to increase the radial ion flux in order to satisfy current density neutrality to the wall. Under the solenoids, the V_p profiles increase from center to edge, which results in a slight radial confinement of the ions. This time, combining the T_e profiles under the solenoids with V_p results in an increase in V_f with r , i.e., there is a significant positive wall charging under the solenoids. This was confirmed with LP measurements, which are not reported here.

The T_e profiles in Figs. 7(c) and 7(d) show interesting axial and radial variations. The temperature remains relatively constant on axis between the antenna and the solenoids, as previously reported,^{19,34} validating the choice of using the mean axial T_e in Fig. 4. Under the antenna, the electron temperature increases by 1.5 eV from center to edge, supporting the operation of *Huia* in E/H mode in which most of the rf power is given to the electrons within the skin depth layer under the antenna.¹⁹ Indeed, with densities of $n_i \simeq 8 \times 10^{10}$ cm⁻³ at the edges of the radial profiles under the antennae, the rf skin depth $\delta = c / (2\pi 9000 \sqrt{n_i}) \simeq 1.9$ cm, where c is the vacuum speed of light.²³ Under the solenoids, T_e radially increases by ~ 1 eV, peaking at the location of the most outward field lines connecting the solenoids with the antenna before dropping by ~ 4.5 eV at the edges of the glass tube. The axial and radial magnitudes of the electron temperatures measured here are similar to those measured with a compensated probe by Bennet *et al.*¹⁹ This indicates that the lack of rf compensation on the LP used here might only have minor effects.

The close match of T_e between $z = 0$ cm and $z = z_B$ on axis and at the location of the connecting field lines is a strong indication that hot electrons are efficiently channeled along the magnetic field lines from the antenna region to the solenoids. Moreover, the cold electron population (i.e., $T_e < 5.5$ eV) lies outside of the magnetic funnel, which gives access to the antenna region. These differentiated electron populations are represented as colored regions in Fig. 5. This effect, combined with the electrostatic acceleration of the electrons by the axial V_p gradient, could explain the high-density peak under the solenoids through localized ionization. The lifetime of excited atoms is indeed less than a few microseconds and the ion-neutral charge-exchange collision mean free path is ~ 2.5 cm. The transport of hot electrons along field lines has been previously reported and was associated with high-density conics forming on these lines.^{12,14,15} An alternative explanation for the presence of hot electrons away from the antenna region would be the existence of a wave-heated regime in *Huia*, of which no sign has been observed so far nor previously reported on *Echidna* (see Sec. IV A).¹⁹

D. Boltzmann relation validation

The existence of different electron populations along separate magnetic field lines can be tested with the Boltzmann relation. It relates the plasma density to a change in plasma potential in the case of an isothermal electron population,

$$n_i(r, z) = n_{ik} \exp\left(\frac{V_p(r, z) - V_{pk}}{kT_e}\right), \quad (2)$$

where n_{ik} and V_{pk} are the known plasma density and potential at a location of reference (r_k, z_k), while $V_p(r, z)$ is the measured plasma potential at the location of interest (r, z). Because the electrons are

tightly held along the field lines and their mean free paths are longer than the glass tube, the spatial distribution of T_e should exhibit isotherms coinciding with the magnetic field lines.³⁴ If this was the case, the Boltzmann relation would be valid along the field lines but not across them.³⁵ Figure 4(d) reports the Boltzmann relation on axis for the loop antenna, using the V_p profile in Fig. 6 and the known plasma density and potential at $(r = 0 \text{ cm}, z = z_B)$. The Boltzmann density profile matches closely the measured profile, with a small overestimation of the density upstream of the peak that could be caused by local ionization. This agreement further supports that T_e can be taken as constant on axis, since Eq. (2) is only valid for an isothermal electron population. This is also corroborated by the similar values of T_e measured between the two axial positions in Fig. 7. As a counterexample, Fig. 7(b) shows the Boltzmann relation of the radial density profile under the solenoids, where electrons are most strongly magnetized ($r_{Le} \simeq 0.19 \text{ mm}$). The difference between the Boltzmann relation and the measured radial densities, while good agreement was obtained on axis, supports the idea that different electron populations exist along field lines with different radial coordinates.

E. Regime transition

The loop antenna axial extent of 0.5 cm allows a more precise characterization of the regime transition compared to the 19 cm of the DS antenna. As stated previously, the ion Larmor radius under the antenna would equal the glass tube radius at critical positions $z_B \simeq -32.4 \text{ cm}$ for 300 G, and $z_B \simeq -41.7 \text{ cm}$ for 600 G.

Figure 8 shows the axial density profiles for small steps of z_B at 300 (a) and 600 G (b). At 300 G, it can be seen that the $z_B = -30 \text{ cm}$ curve is monotonically decreasing with increasing z from its global maximum and has no inflection point where the curve changes from being convex to concave. For $z_B = -31 \text{ cm}$, an inflection point starts to appear at $z \simeq -7 \text{ cm}$. For $z_B = -32$ and $z_B = -33 \text{ cm}$, a density bulge under the antenna appears and the inflection points are well-marked. The bulge under the antenna only becomes a local maximum for $z_B = -38 \text{ cm}$. When z_B passes the critical value, the building up of density under the antenna adds up to the density profile under the solenoids. This can be visualized as the superposition of two axially offset bell-shaped density profiles, with the one representing the antenna having a much smaller magnitude than the solenoids one. The emergence of the antenna “bell” can be characterized by the total density profile exhibiting an inflection point between the solenoids and the antenna. If this is assumed to be the manifestation of regime transition, then it would take place at $z_B \simeq -31 \text{ cm}$ for 300 G. The calculation of r_{Li} assumed a uniform population of ions at room temperature, while in reality $v_{ith} = 394 \text{ m/s}$ is likely to be a lower limit as some localized ion heating processes could be present in *Huia*. The regime transition occurring for $z_B = -31 \text{ cm}$ instead of -32.4 cm could be a sign of such processes. For the 600 G case in Fig. 8(b), applying the same argument shows a regime transition happening between $z_B = -40 \text{ cm}$ and -42 cm . Since the inflection point is already well marked for $z_B = -42 \text{ cm}$, it appears that the transition happens at $z_B \simeq -41 \text{ cm}$.

Figure 9 displays the loop antenna (r, z) maps of I_{sat} for $z_B = -30$ and $z_B = -40 \text{ cm}$ at 300 and 600 G. The $z_B = -40 \text{ cm}$, 300 G (b) map shows that the double peak is a spatial feature that extends beyond the axis, while the transition to the single peak mode at 600 G (d) is complete over the entire (r, z) space.

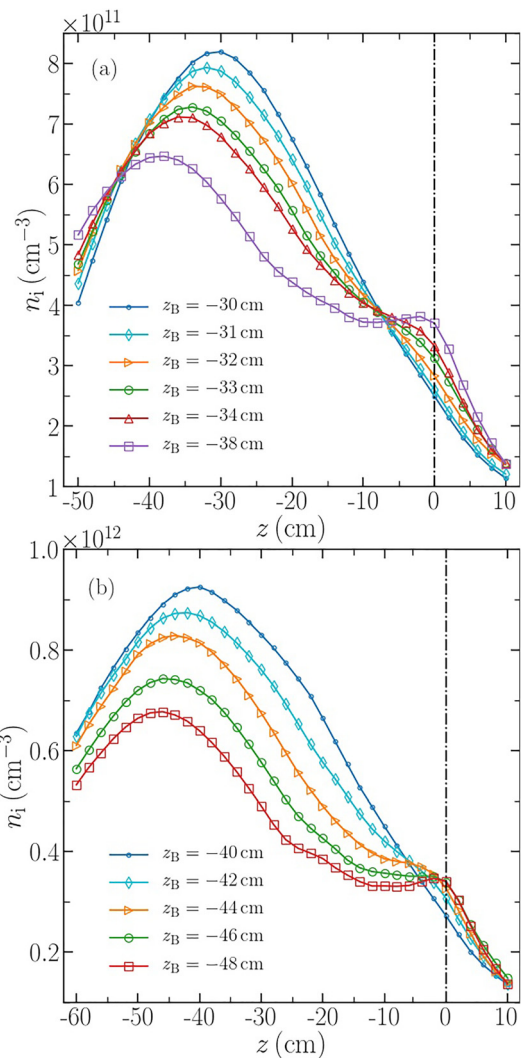


FIG. 8. Loop antenna axial ion density profiles for increasing z_B , showing the transition between the single peak regime and double peak regime for a maximum of B_z of 300 (a) and 600 G (b).

F. Cross-field diffusion

The thick magnetic field line in Fig. 9 shows the most radially outward field line connecting the solenoid region to the surface under the loop antenna, from $r = 4.5 \text{ cm}$ to 1.7 cm . This magnetic funnel sees its cross section reduced by a factor of 7 and the plasma constrained within the funnel would experience a density increase by the same factor under perfect magnetic confinement, i.e., without cross-field diffusion, and in the absence of plasma ionization taking place inside the funnel. Therefore, the quality of the magnetic field confinement can be quantified by comparing the plasma densities between the entrance and the throat of the magnetic nozzle. If local plasma creation is significant and with no cross-field diffusion, this comparison would show a density increase larger than the fraction of geometrical cross-section reduction. For the double-saddle antenna, since it

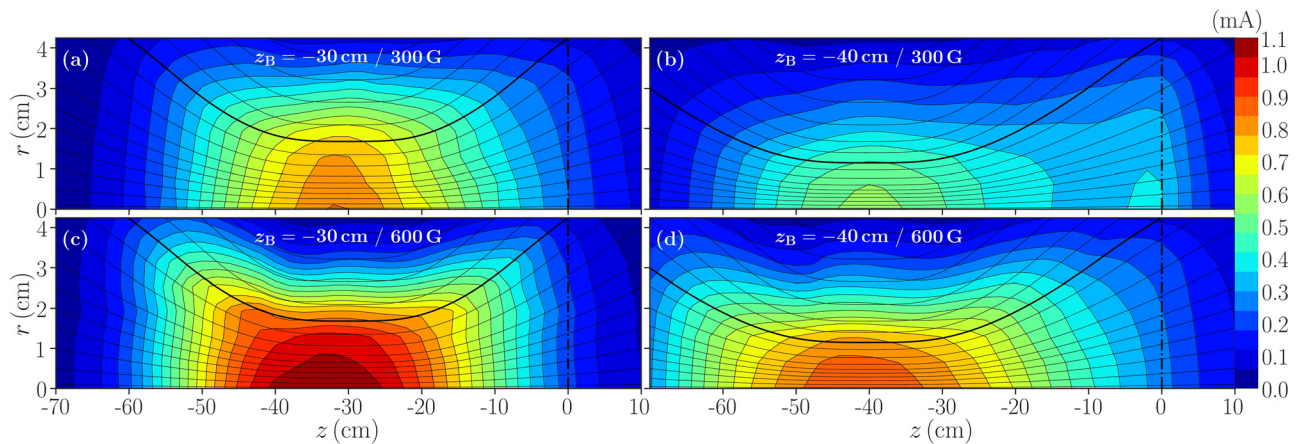


FIG. 9. Two-dimensional ion saturation current maps obtained for $z_B = -30$ cm (a) and (c) and $z_B = -40$ cm (b) and (d), for 300 G (a) and (b) and 600 G (c) and (d). The vertical dot-dashed lines mark the position of the loop antenna, and the thick black continuous line marks the most radial field line which intersects the antenna region. The case $z_B = -40$ cm and 300 G shows that the double peak regime is a volumetric feature. Each map is interpolated from 328 data points.

extends 9 cm further downstream than the loop antenna, the magnetic funnel cross section, is reduced by a factor of 3 only. Examining the densities on axis under the antenna and under the solenoids in Figs. 7(a) and 7(b), one can see that the density increases by factor of ~ 3.3 for both the DS and loop antennae. The DS antenna density increase is in good agreement with the column cross-section reduction, while the discrepancy for the loop antenna case highlights a lower magnetic confinement.

Cross-field diffusion occurs from collisions and electron pressure $p_e = kT_e n_e$ pushing radially outward due to the density and electron temperature both radially decreasing under the solenoids (see Fig. 7). The electron pressure profiles are similar between the DS and loop antennae. However, in the case of the loop antenna, the magnetic field acts to compress the electrons into a smaller volume than with the DS antenna, so that obtaining the expected amount of density increase (factor 7) without cross-field diffusion would require a higher magnetic field. Comparing Fig. 9(a) with Fig. 9(c), it can be seen that the cross-field diffusion is reduced with an increase in magnetic field intensity. The ion saturation current above the thick magnetic field line is higher for 300 G compared to 600 G, while I_{sat} under the solenoids is higher at 600 G. At the same time, I_{sat} under the antenna has not changed significantly and the magnetic confinement has increased. Table II shows the densities under the antenna and under the solenoids ($z_B = 30$ cm) for magnetic field strengths of 300, 600, and 900 G. The density under the antenna shows no significant change with the magnetic field strength, while the density at z_B significantly increased. The ratio of axial density increase in 5.32 for 900 G is closer

TABLE II. Ion densities under the antenna, under the solenoids placed at $z_B = 30$ cm, and their ratios for increasing applied magnetic field strengths.

| B_{z_B} (G) | $n_i(0)$ (cm^{-3}) | $n_i(z_B)$ (cm^{-3}) | $n_i(z_B)/n_i(0)$ (-) |
|---------------|-------------------------------|---------------------------------|-----------------------|
| 300 | 0.22×10^{12} | 0.72×10^{12} | 3.3 |
| 600 | 0.20×10^{12} | 1.01×10^{12} | 5.0 |
| 900 | 0.22×10^{12} | 1.16×10^{12} | 5.3 |

to the expected ratio of 7 as a result of reduced cross-field diffusion and/or increased local plasma creation. Blue core discharges were obtained for both 600 and 900 G with densities $\geq 10^{12} \text{ cm}^{-3}$.

Also visible in Fig. 9(c) are high-density conics on either sides of the solenoids, visible in the form of higher density contours following the thick black magnetic field line. This is additional evidence that the hot electrons heated under the antenna are traveling beyond $z = -50$ cm and could be responsible for remote ionization on each sides of the solenoids. It is also noticeable that these conics are appearing for magnetic fields above 600 G and are more pronounced with increasing field strength.

V. DISCUSSION AND CONCLUSIONS

The design and operation of *Huia*, a new linear magnetized rf plasma device, have been presented. *Huia* has been validated as being suited to continue research on non-local ionization inside a magnetic nozzle.¹⁹ The same two regimes of operations that depend on the separation between the antenna and the solenoids have been observed to occur under the same conditions as in *Echidna*, despite the difference in operating radio frequency.

Extensive efforts were first made to ensure that the newly designed *in situ* diagnostic system presented the least possible disturbance to the plasma. Over the entire range of available parameters, *Huia* appears to be operating as a predominantly capacitive and/or inductive discharge, depending on the applied rf power, magnetic field and argon pressure. Similarly to *Echidna*, no sign of a wave heated regime has been observed, despite the presence of a blue core and densities in excess of 10^{12} cm^{-3} at medium rf powers and magnetic field strengths, i.e., $P_{\text{rf}} \simeq 200$ W and $B_{z_B} \simeq 600$ G. Moreover, the modes of plasma heating seem to have little influence on the regime transition, as its properties remain constant whether *Huia* is working in either E or H mode, or if a loop antenna is used instead of the double-saddle antenna. The use of the loop antenna improved the identification of the regime transition, observed to be starting ≤ 2 cm before the solenoids' position predicted assuming ions at room temperature. Given the simplicity of this assumption, these observations bring further

confidence that the transition is owing to the change in ion magnetization under the antenna.

The differential charging of the glass tube between the antenna and the solenoid region discussed in Sec. IV C also confirms observations made by Bennet *et al.*¹⁹ in *Echidna*. It corroborates a hypothesis that explains how electrons overcome the magnetic mirror adiabatic reflection owing to the differential charging of the wall, which would take place during the initial settling time of the discharge. The new two-dimensional maps of the ion saturation current revealed the presence of high-density conics which coincide with the magnetic flux tubes containing hot electron populations warmed up a few skin-depths under the antenna. This observation supports the existence of an off-axis peak in the radial profiles of the temperature under the solenoids reported in Sec. IV C. The peak location and amplitude confirm that hot electrons are transported from the antenna along the magnetic field lines. This has been previously observed in other rf plasma devices working with converging-diverging magnetic field geometries.^{12–14} The roles of the degree of ion magnetization and plasma confinement for the existence of high density conics and axial densities greater than 10^{12} cm^{-3} can serve as guidelines for design optimization of thruster concepts employing magnetic nozzles. Indeed, extended density conics and high plasma densities at the throat of a MN have been linked to thrust generation processes and thruster efficiency.^{10,15,16}

To overcome the potential limitations of using an uncompensated cylindrical Langmuir for the measurements of T_e , a rf compensated LP paired with analog differentiators is currently being tested to allow more robust 2D measurements of T_e and of the electron energy distribution function using the Druyvesteyn methods.²² This will be used to focus on the magnetic confinement processes, electron transport and cooling mechanisms in *Huia*. Complete two-dimensional maps of V_p at different z_B will bring further characterization of the mode transition, focusing, in particular, on the wall charging of the glass tube. The puzzling observation that both plasmas in *Echidna* and *Huia* establish an axial electrostatic force which compensates the magnetic mirror force will also be investigated by varying the magnetic mirror gradient on axis and comparing it to the axial change in V_p . Finally, it will be interesting to test for the presence of helicon waves in *Huia*, taking advantage of the variable working frequency and choice of antenna to tune the device into conditions fulfilling the helicon dispersion relation in non-uniform plasma densities.³⁶

ACKNOWLEDGMENTS

The authors wish to acknowledge S. Warrington and G. Brant from the University of Auckland Technical Services Workshop for their expertise in helping us building *Huia*. This work is partly supported by a New Zealand Space Agency research contract (MBIE No. 00008060).

AUTHOR DECLARATIONS

Conflict of Interest

The authors have no conflicts to disclose.

DATA AVAILABILITY

The data that support the findings of this study are available from the corresponding author upon reasonable request.

REFERENCES

- R. W. Boswell, "Very efficient plasma generation by whistler waves near the lower hybrid frequency," *Plasma Phys. Controlled Fusion* **26**, 1147 (1984).
- F. F. Chen, "Experiments on helicon plasma sources," *J. Vac. Sci. Technol. A* **10**, 1389–1401 (1992).
- T. Fowler, "Fusion research in open-ended systems," *Nucl. Fusion* **9**, 3 (1969).
- C. Marini, R. Agnello, B. Duval, I. Furno, A. Howling, R. Jacquier, A. Karpushov, G. Plyushchev, K. Verhaegh, P. Guittienne, U. Fantz, D. Wunderlich, S. Béchu, and A. Simonin, "Spectroscopic characterization of H₂ and D₂ helicon plasmas generated by a resonant antenna for neutral beam applications in fusion," *Nucl. Fusion* **57**, 036024 (2017).
- R. W. Boswell, E. Marsch, and C. Charles, "The current-free electric double layer in a coronal magnetic funnel," *Astrophys. J. Lett.* **640**, L199 (2006).
- P. Shi, P. Srivastav, C. Beatty, R. John, M. Lazo, J. McKee, J. McLaughlin, M. Moran, M. Paul, E. E. Scime, E. E. Scime, D. Thompson, and T. Steinberger, "Alfvénic modes excited by the kink instability in plasma," *Phys. Plasmas* **28**, 032101 (2021).
- S. Mazouffre, "Electric propulsion for satellites and spacecraft: Established technologies and novel approaches," *Plasma Sources Sci. Technol.* **25**, 033002 (2016).
- C. Charles and R. Boswell, "Current-free double-layer formation in a high-density helicon discharge," *Appl. Phys. Lett.* **82**, 1356–1358 (2003).
- K. Takahashi, "Magnetic nozzle radiofrequency plasma thruster approaching twenty percent thruster efficiency," *Sci. Rep.* **11**, 1–12 (2021).
- K. Takahashi, C. Charles, and R. W. Boswell, "Approaching the theoretical limit of diamagnetic-induced momentum in a rapidly diverging magnetic nozzle," *Phys. Rev. Lett.* **110**, 195003 (2013).
- K. Takahashi, C. Charles, R. W. Boswell, and A. Ando, "Thermodynamic analogy for electrons interacting with a magnetic nozzle," *Phys. Rev. Lett.* **125**, 165001 (2020).
- C. Charles, "High density conics in a magnetically expanding helicon plasma," *Appl. Phys. Lett.* **96**, 051502 (2010).
- S. Saha, S. Chowdhury, M. Janaki, A. Ghosh, A. Hui, and S. Raychaudhuri, "Plasma density accumulation on a conical surface for diffusion along a diverging magnetic field," *Phys. Plasmas* **21**, 043502 (2014).
- K. Takahashi, H. Akahoshi, C. Charles, R. W. Boswell, and A. Ando, "High temperature electrons exhausted from rf plasma sources along a magnetic nozzle," *Phys. Plasmas* **24**, 084503 (2017).
- A. Bennet, C. Charles, and R. Boswell, "Selective radial release of hot, magnetized electrons downstream of a low-pressure expanding plasma," *J. Phys. D: Appl. Phys.* **51**, 375204 (2018).
- A. Bennet, C. Charles, and R. Boswell, "Separating the location of geometric and magnetic expansions in low-pressure expanding plasmas," *Plasma Sources Sci. Technol.* **27**, 075003 (2018).
- X. M. Guo, J. Scharer, Y. Mouzouris, and L. Louis, "Helicon experiments and simulations in nonuniform magnetic field configurations," *Phys. Plasmas* **6**, 3400–3407 (1999).
- B. D. Blackwell, J. F. Caneses, C. M. Samuell, J. Wach, J. Howard, and C. Corr, "Design and characterization of the Magnetized Plasma Interaction Experiment (MAGPIE): A new source for plasma-material interaction studies," *Plasma Sources Sci. Technol.* **21**, 055033 (2012).
- A. Bennet, C. Charles, and R. Boswell, "Non-local plasma generation in a magnetic nozzle," *Phys. Plasmas* **26**, 072107 (2019).
- J. Simpson, J. Lane, C. Immer, and R. Youngquist, "Simple analytic expressions for the magnetic field of a circular current loop," NASA Technical Report No. NASA/TM-2013-217919 (NASA, 2001).
- R. L. Merlino, "Understanding Langmuir probe current-voltage characteristics," *Am. J. Phys.* **75**, 1078–1085 (2007).
- V. Godyak, R. Piejak, and B. Alexandrovich, "Measurement of electron energy distribution in low-pressure rf discharges," *Plasma Sources Sci. Technol.* **1**, 36 (1992).
- M. A. Lieberman and A. J. Lichtenberg, *Principles of Plasma Discharges and Materials Processing* (John Wiley & Sons, New York, 2005), pp. 165–206.

- ²⁴P. Chabert and N. Braithwaite, *Physics of Radio-Frequency Plasmas* (Cambridge University Press, 2011).
- ²⁵I. D. Sudit and F. F. Chen, “RF compensated probes for high-density discharges,” *Plasma Sources Sci. Technol.* **3**, 162 (1994).
- ²⁶Y. Zhang, C. Charles, and R. W. Boswell, “Density measurements in low pressure, weakly magnetized, rf plasmas: Experimental verification of the sheath expansion effect,” *Front. Phys.* **5**, 27 (2017).
- ²⁷J. Sheehan and N. Hershkowitz, “Emissive probes,” *Plasma Sources Sci. Technol.* **20**, 063001 (2011).
- ²⁸A. Caldarelli, F. Filleul, C. Charles, N. Rattenbury, and J. Cater, “Preliminary measurements of a magnetic steering system for rf plasma thruster applications,” in *AIAA Propulsion and Energy 2021 Forum* (American Institute of Aeronautics and Astronautics, 2021), p. 3401.
- ²⁹A. Degeling, C. Jung, R. Boswell, and A. Ellingboe, “Plasma production from helicon waves,” *Phys. Plasmas* **3**, 2788–2796 (1996).
- ³⁰M. Lieberman and R. Boswell, “Modeling the transitions from capacitive to inductive to wave-sustained rf discharges,” *J. Phys. IV* **8**, Pr7–145 (1998).
- ³¹J. Hopwood, C. Guarnieri, S. Whitehair, and J. Cuomo, “Langmuir probe measurements of a radio frequency induction plasma,” *J. Vac. Sci. Technol. A* **11**, 152–156 (1993).
- ³²T. Zhang, R. Cui, W. Zhu, Q. Yuan, J. Ouyang, K. Jiang, H. Zhang, C. Wang, and Q. Chen, “Influence of neutral depletion on blue core in argon helicon plasma,” *Phys. Plasmas* **28**, 073505 (2021).
- ³³F. F. Chen, *Introduction to Plasma Physics and Controlled Fusion* (Springer, 1984), Vol. 1.
- ³⁴C. Samuelli, B. Blackwell, J. Howard, and C. Corr, “Plasma parameters and electron energy distribution functions in a magnetically focused plasma,” *Phys. Plasmas* **20**, 034502 (2013).
- ³⁵A. Bennet, C. Charles, and R. Boswell, “Field-aligned Boltzmann electric triple layer in a low-pressure expanding plasma,” *Plasma Sources Sci. Technol.* **28**, 06LT01 (2019).
- ³⁶P. Guittienne, R. Jacquier, B. P. Duteil, A. A. Howling, R. Agnello, and I. Furno, “Helicon wave plasma generated by a resonant birdcage antenna: Magnetic field measurements and analysis in the RAID linear device,” *Plasma Sources Sci. Technol.* **30**, 075023 (2021).